Extreme Mechanics Letters 83 (2026) 102458

Contents lists available at ScienceDirect

Extreme Mechanics Letters

journal homepage: www.elsevier.com/locate/eml

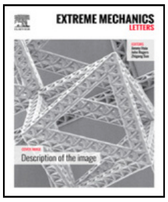

Blister deformation and interlayer delamination in shaft-loaded bilayer films

Ce Sun, Jian Sun, Jinsong Leng *

Centre for Composite Materials and Structures, Harbin Institute of Technology (HIT), No. 2 YiKuang Street, Harbin, 150080, China

ARTICLE INFO

Keywords:
Bilayer
Films
Delamination
Bilayer peeling
Blister deformation
Interlayer debonding

ABSTRACT

Bilayer and multilayer films enhance functional performance through the designed property differences between their constituent layers, leading to their widespread application. The adhesive interface is crucial for stress transfer and for predicting structural delamination and deformation. This study investigates the blister deformation and subsequent delamination of a bilayer film subjected to shaft loading. A theoretical framework combining nonlinear elasticity and Griffith's energy theory is developed to predict the film's behavior. Finite element simulations and physical experiments are conducted to validate the theoretical predictions. Finally, we analyze the effects of different modulus ratios and pre-stretched conditions on deformation and delamination, providing insights for designing and optimizing bilayer film systems.

1. Introduction

Thin films are fundamental to numerous natural and engineered systems. Moving beyond single-layer designs, bilayer and multilayer structures provide expanded functionality by combining layers with distinct properties. These advanced films have found significant applications in fields such as biomedical engineering [1,2], flexible electronics [3,4], and aerospace [5]. An exemplary application is the bilayer Janus dressing [6,7], consisting of thin films with different functionalities: the tissue-facing side is typically hydrophilic to promote adhesion and interfacial compatibility, while the outer side is rendered hydrophobic to minimize adhesion to surrounding tissues [6,7]. Interface between layers governs stress transfer, as a key determinant of safety and performance in bilayer and multilayer films [8]. Hence, understanding the interfacial adhesion and deformation behavior of bilayer film structures is essential for guiding their design.

Kendall's foundational work on film peeling has promoted the research into theoretical models of peeling [9]. Recent work has incorporated hyperelasticity [10,11], viscoelasticity [12,13], plasticity [14–17], pre-stretched [18], and friction [19] into peeling analyses. However, most theories remain focused on single-layer films, while many applications (such as laminated Janus dressings [20,21] and transfer printing of flexible electronics [22,23]) involve bilayer or multilayer films. Theoretical models addressing the delamination and deformation of bilayer films remain relatively limited and are largely restricted to two-dimensional analyses of slender-tape geometries. For example, in recent work, Yin et al. [22] develops a two-dimensional model based on small-deformation theory and cohesive-zone theory to analyze the competitive delamination between bilayer tape films and substrates, deriving an analytical expression for the interaction-zone length and conducting an in-depth theoretical investigation of delamination in the context of film transfer, considering bending stiffness, interfacial toughness, and interfacial strength. Prior to Yin et al. two frameworks had been established: (i) cohesive-zone models to describe fracture-path selection (Jain et al. [24]; Yin et al. [25]; Jian et al. [23]); (ii) energy-method frameworks based on variational analyses of strain energy in deformed bilayers (Heide et al. [26]; Shen et al. [27,28]). These approaches prove effective for slender-tape bilayers, with the former highlighting fracture strength and mode effects and the latter capturing large deformations.

A typical feature of slender-tape film peeling is that the delamination front forms a straight line, reducing the problem to a two-dimensional delamination analysis. However, for multilayer film structures such as Janus bilayer dressings, realistic loading conditions often yield localized or nonuniform stresses on the film, giving rise to three-dimensional debonding phenomena. At present, most theoretical studies of three-dimensional peeling of thin films assume single-layer peeling from a rigid substrate [29,30]. Research specifically addressing three-dimensional debonding in bilayer films remains relatively limited. Therefore, in this work we investigate the three-dimensional deformation and interfacial delamination behavior of bilayer films under localized loading, with the aim of providing theoretical guidance for the design of bilayer film systems.

This work proceeds as follows. We establish the theoretical framework for the deformation and delamination of bilayer films in Section 2.

---

* Corresponding author.
E-mail address: lengjs@hit.edu.cn (J. Leng).

https://doi.org/10.1016/j.eml.2026.102458
Received 3 November 2025; Received in revised form 5 January 2026; Accepted 6 February 2026

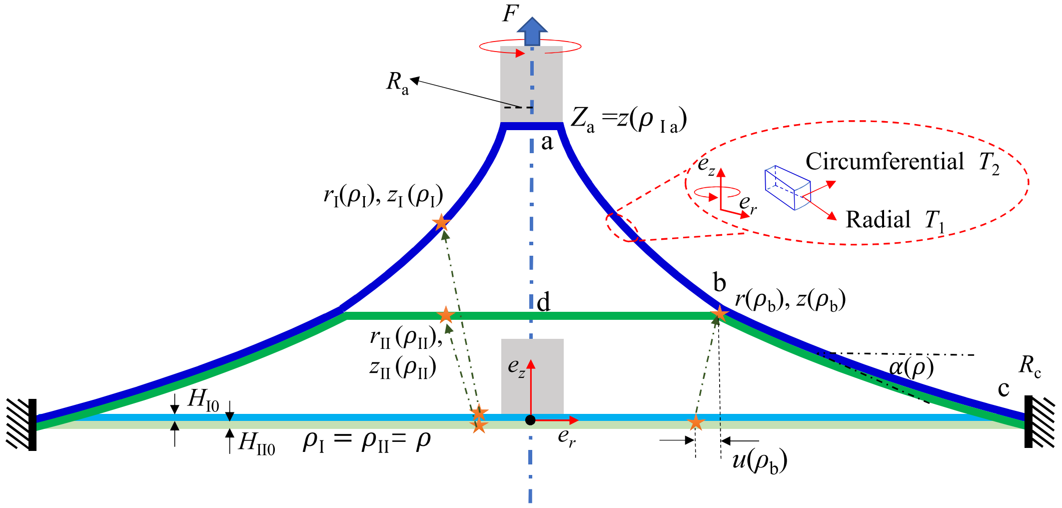

Fig. 1. Schematic diagram of the theoretical model. The axisymmetric bilayer films are fixed at the outer boundaries. The center of the upper film is connected to a flat indenter. When a vertical displacement is applied to the indenter, the bilayer membrane will deform and delaminate. H_{I0} and H_{II0} are initial thicknesses of the upper and lower films. R_c are the radius of two films. Z_a is the platen vertical displacement and $\bar{Z}_a = \frac{Z_a}{R_c}$. ρ_b is the material coordinate at the debonding point and $\bar{\rho}_b = \frac{\rho_b}{R_c}$. $u(\rho_b)$ is the radial displacement of debonding point and $\bar{u}(\rho_b) = \frac{r_b - \rho_b}{R_c}$.

Section 3 validates the model and investigates the effects of film modulus and pre-stretched on deformation and interfacial delamination. Section 4 provides experiment. Section 5 provides the conclusions.

2. Theoretical analysis

This section presents a theoretical model, as shown in Fig. 1, which includes two films with radius R_c and fixed outer boundaries. The upper and lower films have initial thicknesses H_{I0} and H_{II0}, respectively. Additionally, a rigid platen of radius R_a is centrally attached to the upper film. Platen vertical displacement Z_a induces deformation in the films, with potential delamination depending on the material and adhesion properties. The films are modeled as incompressible hyperelastic continua described by the neo-Hookean constitutive relation. The model is established under axisymmetric conditions, where ρ represents the radial material coordinate, defined as the distance from a material point to the film center. In the initial configuration, with $\rho_{\mathrm{I}} = \rho_{\mathrm{II}} = \rho$, allowing omission of the subscripts. In the current configuration, the upper film segment ab has radial and vertical coordinates $r_{\mathrm{I}}(\rho_{\mathrm{I}})$ and $z_{\mathrm{I}}(\rho_{\mathrm{I}})$ respectively; the lower film segment bd by $r_{\mathrm{II}}(\rho_{\mathrm{II}})$ and $z_{\mathrm{II}}(\rho_{\mathrm{II}})$; and the non-delamination segment bc by $r(\rho)$ and $z(\rho)$. The angle between the film tangent and the horizontal direction is denoted by $\alpha(\rho)$. Upon interfacial debonding, the material coordinate at the debonding point, ρ_b, defines the delamination radius.

2.1. Governing equations for films deformation

This section derives the governing equations of film in segments ab and bc. The governing equations are the same for both segments and subscripts are omitted to simplify the notation. In the deformed state, let λ_1, λ_2, and λ_3 denote the principal stretches in the radial, circumferential, and through-thickness directions, respectively.

$$\lambda_1 = \sqrt{r'^2 + z'^2}, \lambda_2 = \frac{r}{\rho}, \lambda_3 = \frac{h}{H}, \tag{1}$$

where h and H is the deformed and undeformed thickness of the membrane and if the two layers have the same initial thickness, $H = H_{\mathrm{I0}} = H_{\mathrm{II0}}$. The corresponding curvatures are κ_1 and κ_2, defined as

$$\kappa_1 = \frac{\alpha'}{\lambda_1}, \kappa_2 = \frac{\sin\alpha}{r\lambda_2}. \tag{2}$$

The prime ($'$) denotes differentiation with respect to the material coordinate ρ. The tangent angle α can be

$$\alpha = \arctan\left(\frac{z'}{r'}\right) \tag{3}$$

In an incompressible neo-Hookean film, strain energy density is [31,32]

$$W = \frac{\mu}{2}\left(\lambda_1^2 + \lambda_2^2 + \lambda_3^2 - 3\right), \tag{4}$$

in which μ is shear modulus. The Cauchy stresses in the radial and circumferential directions are [33]

$$\begin{aligned} T_1 &= h\lambda_1\left(\frac{\partial W}{\partial \lambda_1}\right), \\ T_2 &= h\lambda_2\left(\frac{\partial W}{\partial \lambda_2}\right). \end{aligned} \tag{5}$$

For incompressible material, the volume stretch must satisfy $\lambda_1\lambda_2\lambda_3 = 1$. By substituting Eqs. (1), (4) into (5), we can obtain

$$\begin{aligned} T_1 &= \mu H\left(\frac{\lambda_1}{\lambda_2} - \frac{1}{\lambda_1^3\lambda_2^3}\right), \\ T_2 &= \mu H\left(\frac{\lambda_2}{\lambda_1} - \frac{1}{\lambda_1^3\lambda_2^3}\right), \end{aligned} \tag{6}$$

Assuming that the thickness of the membrane with respect to the radius $\frac{h}{R_c}$ is small and large tensile forces occur in the membrane during deformation, so we can neglect the bending stiffness and bending stresses and use the theory of non-linear elastic membranes [34,35]. The equilibrium equations are [36]

$$(rT_1)' - r'T_2 = 0, \tag{7}$$

$$\kappa_1 T_1 + \kappa_2 T_2 = 0. \tag{8}$$

Further discussion on the nonlinear elastic membranes theory used in this study can be found in Appendix A.

The equation is first solved for segment ab, then combined with the force equilibrium equation at point b, and subsequently solved for segment bc. Appendix B provides detailed boundary condition settings and methods for solving the differential equations.

2.2. Delamination of the films

The previous theory assumes no delamination occurs in segment bc. The previous theory assumes no delamination occurs in segment bc. If delamination occurs, the delamination front at b propagates to the right as the vertical displacement increases. The delamination problem can be analyzed by Griffith energy theory. Under the displacement control mode, the energy release rate is expressed as [37]

$$G = -\frac{\partial U_e}{\partial s}, \tag{9}$$

where s denotes the delamination propagation area, which is given by $s = \pi\rho_b^2$. The total strain energy U_e is

$$U_e = \int_{\rho_{\mathrm{Ia}}}^{\rho_{\mathrm{Ib}}} 2\pi\rho_{\mathrm{I}} H_{\mathrm{I0}} W(\rho_{\mathrm{I}}) d\rho_{\mathrm{I}} + \int_{0}^{\rho_{\mathrm{IIb}}} 2\pi\rho_{\mathrm{II}} H_{\mathrm{II0}} W(\rho_{\mathrm{II}}) d\rho_{\mathrm{II}} + \int_{\rho_b}^{\rho_c} 2\pi\rho (H_{\mathrm{I0}} + H_{\mathrm{II0}}) W(\rho) d\rho. \tag{10}$$

According to the Griffith energy theory, delamination propagation will occur when $G \geq G_c$ and G_c is the critical energy release rate. In our analysis, we assume the peeling process is steady-state, and the crack propagates in a stable manner, so that $G_c = G = -(\partial U_e)/\partial s$.

3. Results and discussion

3.1. Deformation of bilayer films

In this section, we consider two identical films with equal thickness and modulus ($H_{\mathrm{I0}} = H_{\mathrm{II0}}$ and $\mu_{\mathrm{I}} = \mu_{\mathrm{II}}$). Relevant variables during deformation are nondimensionalized using R_c and H_{I0} as the characteristic length and thickness, respectively,

$$\bar{Z}_a = \frac{Z_a}{R_c}, \quad \bar{\rho}_b = \frac{\rho_b}{R_c}, \quad \bar{u}(\rho_b) = \frac{r_b - \rho_b}{R_c}, \quad \bar{F} = \frac{F}{2\pi\mu_{\mathrm{II}} H_{\mathrm{I0}} R_c},$$
$$\bar{U}_e = \frac{U_e}{\mu_{\mathrm{II}} H_{\mathrm{I0}} R_c^2}, \quad \bar{G} = \frac{G}{\mu_{\mathrm{II}} H_{\mathrm{I0}}}, \tag{11}$$

where $u(\rho_b)$ is the radial displacement of point b and F denotes the vertical force acting on the film, given by

$$F = 2\pi R_a \sin\left(\alpha(\rho_{\mathrm{Ia}})\right) T_1(\rho_{\mathrm{Ia}}). \tag{12}$$

When $\rho_b = 0.5$ is held constant, the profiles of the films at $\bar{Z}_a = 0.2$, 0.3, and 0.4 are in Fig. 2(a). Dashed lines represent theoretical predictions, while points indicate simulations. See the Appendix C for simulation details. A slight difference in segment bd is observed between the theoretical predictions and the simulation, which can be attributed to the theory's neglect of bending effects. Nevertheless, the overall agreement between theory and simulation supports the validity of the proposed theoretical framework. Fig. 2(b) displays the variation of load, while Fig. 2(c) displays strain energy. The points represent theoretical predictions and lines denote simulation results. The theoretical predictions also agree with the simulations. From another perspective, for a constant $\bar{Z}_a$, decreasing $\bar{\rho}_b$ increases both the strain energy and the load. This trend arises because a smaller $\bar{\rho}_b$ corresponds to a larger bilayer region, which enhances the membrane's resistance to deformation. The limiting cases $\bar{\rho}_b = 1$ and $\bar{\rho}_b = 0$ represent deformation of pure single-layer and pure bilayer film, respectively. In fact, the delamination process represents the transition from single-layer film ($\bar{\rho}_b = 1$) to bilayer ($\bar{\rho}_b = 0$).

A critical step in the proposed theoretical framework is enforcing force equilibrium at point b (Eqs. (B.9) and (B.10)). This force balance requires the bd segment film is in tension. The radial displacement at point b for $\bar{\rho}_b = 0.2$, 0.4, 0.6, 1 are shown in Fig. 2(d). Dotted lines and dashed lines denote theoretical predictions and simulation results. The observed discrepancies between theory and simulation may originate from factors such as the omission of bending effects and limitations in computational precision. An importance observation is that $\bar{u}(\rho_b)$ for the bilayer films are consistently positive, which differs from the pure single-layer film case $\bar{\rho}_b = 1$ (solid lines). For $\bar{\rho}_b = 1$, $\bar{u}(\rho_b)$ decreases with increasing $\bar{Z}_a$ and remains negative, indicating a contraction tendency of the single-layer film during deformation. Conversely, for the bilayer film, the radial displacement at points $\frac{\rho}{R_c} = 0.2$, 0.4, 0.6 increases with $\bar{Z}_a$ and remains positive, indicating expansion away from the symmetry axis under vertical loading.

3.2. Effect of modulus ratios

This section investigates the influence of modulus ratios $\bar{\mu}$ on the film deformation, where $\bar{\mu} = \frac{\mu_{\mathrm{I}}}{\mu_{\mathrm{II}}}$. $\bar{\mu} > 1$ represents Harder Upper layer and Softer Lower layer (HU-SL) case, and $\bar{\mu} < 1$ indicates the opposite Softer Upper layer and Harder Lower layer (SU-HL) case.

Fig. 3(a) presents the radial displacement of point b for $\bar{\mu}$ ranging from 0.1 to 10, with $\bar{\rho}_b = 0.4$. For $\bar{\mu} < 1$ (SU-HL), the displacement of point b remains positive, indicating tension in segment bd. Conversely, for $\bar{\mu} > 1$ (HU-SL), the displacement become negative, reflecting compression in the same segment. These findings are corroborated by the stress states at point d shown in Fig. 3(b) and (c). Specifically, Fig. 3(b) and (c) depict the radial stress at point d, where points A–E sequentially represent the radial element stresses from top to bottom. In Fig. 3(b), radial stresses are uniformly positive, indicating tension. However, in Fig. 3(c), at the initial stage of film deformation, a positive radial stress is observed at the top surface (element A), while a negative radial stress appears at the bottom surface (element E), suggesting that the bd segment of the film is subjected to bending. The displacement of point b for $\bar{\rho}_b = 0.2$, 0.6, and 0.8 are shown in Fig. 3(d). For $\bar{\mu} = 0.1$ (SU-HL), the loads are from Eq. (12), with the corresponding values marked by points in Fig. 3(e), where the solid line represents simulation results. The agreement between theory and simulation demonstrates the applicability of theoretical framework to SU-HL bilayer films. However, for $\bar{\mu} > 1$, the theory is limited, as segment bd undergoes compression or bending, which contradicts the assumption of tension in Eq. (B.9). For $\bar{\mu} > 1$, where the lower film is in compression, we propose a simplified analytical approach. In this regime, the significantly softer lower film leads to the deformation predominantly controlled by the harder upper layer, allowing the contribution of segment bd to be neglected. Consequently, Eq. (B.9) can be further simplified as

$$T_1(\rho_{\mathrm{Ib}})\cos(\alpha_{\mathrm{Ib}}) = T_1(\rho_b)\cos(\alpha_b) \tag{13}$$

The corresponding force–displacement curves are presented in Fig. 3(f), where the theoretical predictions are almost agreement with the simulation results.

For $\bar{\mu} \geq 1$, we propose an alternative theoretical method to analyze the deformation of bilayer films. Specifically, we consider the deformation following an initial radial pre-stretched. By applying a pre-stretched λ_{pre} at position c, we solve the governing equations, which yield a positive displacement at point b. $\lambda_{\mathrm{pre}} = 1.05$, 1.1, 1.15, and 1.2 are examined for two cases $\bar{\mu} = 1$ and 10. The force–displacement curves are shown in Fig. 4(a) and (b), and the theory agrees with the simulations. Furthermore, the radial displacement at point b remains positive for both cases, indicating that the bd segment remains in tension.

3.3. Interfacial delamination in bilayer films

According to Eq. (9), U_e should be evaluated as a function of ρ_b at constant Z_a. U_e, calculated using Eq. (10), are shown in Fig. 5(a), where the solid markers denote theoretical results and hollow markers denote simulation results. These results are consistent with those shown in Fig. 2(c), with overall agreement between theory and simulation. A minor discrepancy remains, attributable to the omission of bending effects in the theoretical model. For one fixed $\bar{Z}_a$, $\bar{U}_e$ as a function of $\bar{\rho}_b$ can be fitted by a polynomial. This yields an explicit relationship between ρ_b and U_e. By applying Eq. (9), the energy release rate curves are obtained (Fig. 5(b)). These curves illustrate the relationship between $\bar{G}$ and $\bar{\rho}_b$.

For $\bar{G} = \bar{G}_c = 0.005$, the corresponding delamination radius $\bar{\rho}_b$ for each $\bar{Z}_a$ are obtained from Fig. 5(b) and presented as solid markers in Fig. 5(c). The theoretical framework neglects bending effects, while U_e, which accounts for bending, can be computed through simulation, as indicated by the hollow markers in Fig. 5(a). The corresponding energy release rates, derived from the U_e using Eq. (9), are depicted by the

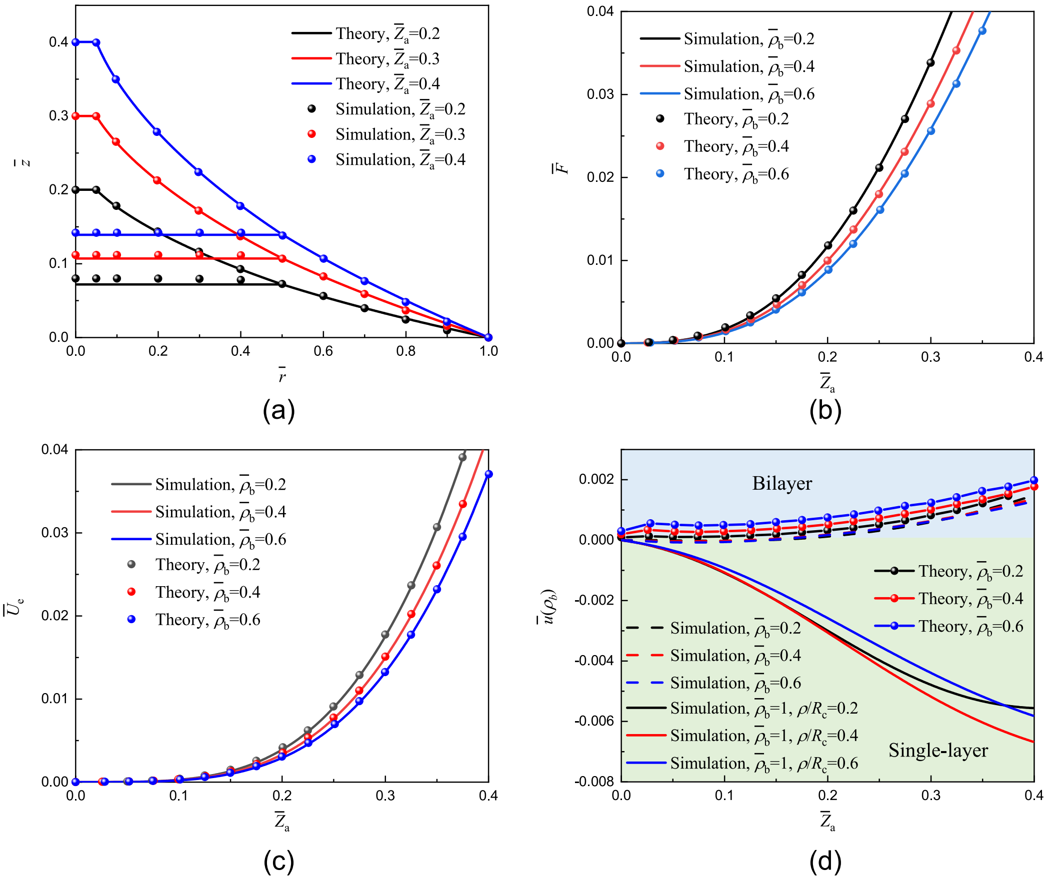

Fig. 2. Comparison of theoretical and simulation results: (a) Profiles of the films at different $\bar{Z}_a$. (b) Load versus $\bar{Z}_a$. (c) Strain energy versus $\bar{Z}_a$. (d) Radial displacement at point b. The solid curves corresponding to the single-layer case exhibit a contraction in the radial direction during deformation.

dashed lines in Fig. 5(b). Similarly, $\bar{\rho}_b$ is obtained and represented by hollow circles in Fig. 5(c), which will be referred to as the approximate results. For comparison, Fig. 5(c) also shows the pure simulation results obtained through the virtual crack-closure technique (VCCT, details in Appendix C), represented by the solid lines. As illustrated in Fig. 5(c), the theoretical predictions are broadly consistent with the simulation, yet discrepancies remain. These mainly arise from three sources: (i) errors in fitting and differentiating the strain energy function; (ii) bending effects, which may cause the approximate results to deviate from the purely theoretical predictions when bending is considered; and (iii) the use of VCCT, whose crack-tip energy release rate estimates, based on linear elasticity, can introduce about a 5% error [38].

Regarding the fracture mode, $\bar{G}$ during the delamination process at $\bar{G}_c = 0.005$ has been calculated, as illustrated in Fig. 5(d). The solid curve represents the total energy release rate $\bar{G}_{\mathrm{equiv}} = \bar{G}_{\mathrm{I}} + \bar{G}_{\mathrm{II}}$, while the dashed curve and dotted curve correspond to mode I and II components, $\bar{G}_{\mathrm{I}}$ and $\bar{G}_{\mathrm{II}}$, respectively. Overall, Fig. 5(d) shows that $\bar{G}_{\mathrm{equiv}}$ remains essentially constant, supporting the assumption $\bar{G} = \bar{G}_c$ for quasi-static case. For further discussion, please refer to the Appendix C. Additionally, we calculated $\bar{F}$ in the delamination process for various $\bar{G}$, as shown in Fig. 5(e). Before complete delamination, changing in interfacial properties significantly affect the force–displacement response, as the interfacial properties determine the extent of delamination.

To investigate the influence of modulus contrast on the delamination behavior of bilayer film structures, we conducted simulations for five modulus ratios $\bar{\mu} = 0.2$, 0.5, 1, 3, and 5, as shown in Fig. 5(f). Solid curves indicate comparatively weak interfacial adhesion, while dashed curves indicate stronger. Stronger interface significantly impedes delamination propagation. For a given interfacial property, a smaller $\bar{Z}_a$ yields larger $\bar{\rho}_b$ in bilayer structures with a lower $\bar{\mu}$; conversely, as $\bar{Z}_a$ increases, bilayer structures with a higher $\bar{\mu}$ exhibit comparatively smaller $\bar{\rho}_b$. These findings can provide qualitative guidance for the design of bilayer films systems. When the interfacial adhesion is weaker and the out-of-plane displacement $\bar{Z}_a$ is smaller, the HU-SL configuration is recommended, as it exhibits a smaller delamination radius for one $\bar{Z}$. From the energy perspective, a substantial portion of the external work is dissipated by bilayer deformation, reducing the tendency for delamination. Conversely, as $\bar{Z}_a$ increases, the trend reverses: the SU-HL exhibits the smaller delamination radius $\bar{\rho}_b$ for the same $\bar{Z}_a$. In this regime, the softer upper film undergoes greater deformation, and most of the out-of-plane displacement is accommodated by the deformation of the delaminated upper layer, thereby reducing the effective load transferred to the bilayer system. Therefore, for large out-of-plane displacements, the SU-HL configuration is preferred.

4. Experiment of interfacial delamination

This section reports experiments on interface delamination. The bilayer film structure is formed by bonding two PDMS films, each with a thickness of 0.5 mm and a radius of 120 mm. The PDMS films were purchased from Juancheng Lileng Technology Co., Ltd. To determine ρ_b, seven concentric circles with radii from 30 to 90 mm (increments of 10 mm) are pre-marked on the surface of the upper film as scale marks. When the debonding front coincides with a circle, that circle's radius is taken as ρ_b; if the front lies between adjacent circles, ρ_b is assigned as the average of the two radii. Therefore, the maximum error of ρ_b is within 10 mm. Prior to testing, the bilayer film assembly is clamped along a circular boundary of radius 100 mm. The center of the upper film is clamped by a hollow platen of radius 5 mm to avoid pressure buildup in the cavity. An initial delamination with radius 5 mm is

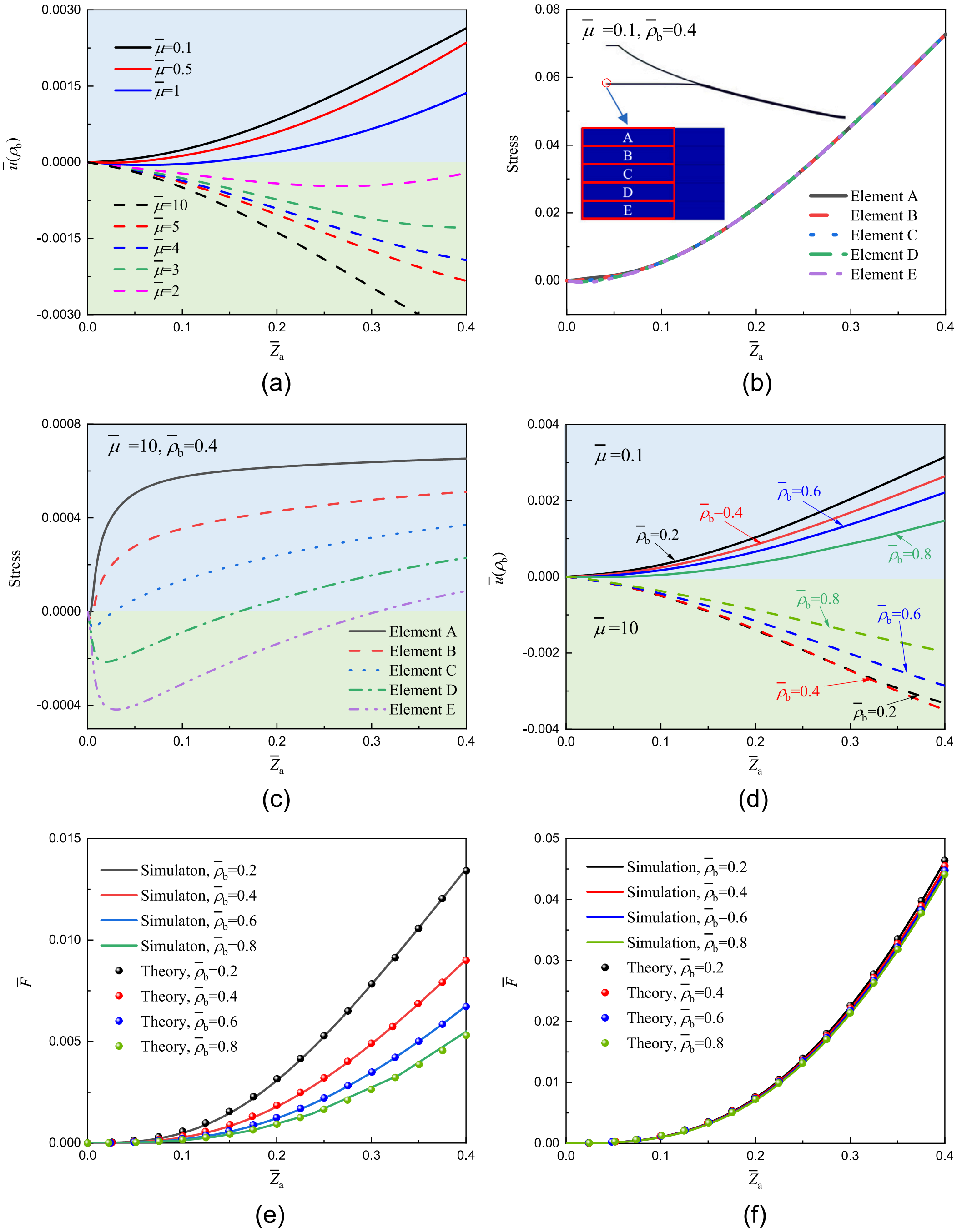

Fig. 3. Effect of modulus on the deformation of bilayer films: (a) $\bar{u}(\rho_b)$ for HU-SL and SU-HL at $\bar{\rho}_b = 0.4$. (b) Element stresses of point d for $\bar{\mu} = 0.1$. (c) Element stresses of point d for $\bar{\mu} = 10$. (d) Displacement of $\bar{u}(\rho_b)$ for $\bar{\rho}_b$ from 0.2 to 0.8. (e) Force–displacement curves for $\bar{\mu} = 0.1$. (f) Force–displacement curves for $\bar{\mu} = 10$.

present between the films. The tensile testing machine Shimadzu AGS-X series (100 N range) was used in the experiment. During testing, a vertical displacement of 0–50 mm is applied to the platen. As the platen translates upward, the film is pulled, and the interfacial crack propagates outward from the prefabricated initial crack.

Fig. 6(a) presents the film profiles for $\bar{Z}_a$ from 0.3 to 0.45. The first row shows the film profiles recorded by the camera, and the second row presents simulation results. At $\bar{Z}_a = 0.30$, $\bar{\rho}_b$ is concentrated around 0.4, with a small region on the film's right side where $\bar{\rho}_b$ slightly exceeds 0.4. The boundary exhibits minor non-circularity. At $\bar{Z}_a = 0.40$, $\bar{\rho}_b$ is distributed between 0.6 and 0.7, and the greater dispersion of $\bar{\rho}_b$ results in more pronounced non-circularity. Taking 0.65 as the effective radius leads to a non-circularity of 15.4%. More results throughout the delamination process can be seen in the Supporting Video.

Fig. 6(b) presents a comparison among experiments, theory, and simulation. For theory and simulation, $\mu = 0.26$ MPa and $\bar{G}_c = 0.00026$ N/mm (Fig. 6(c)) are from experiments in Appendix D. Since the measurement of ρ_b is estimated based on the concentric circles of the film reference marks, there will be a measurement error within 10 mm in the measured value of ρ_b. Therefore, the type B uncertainty of ρ_b is $u_B = \frac{10}{\sqrt{3}}$ mm. For $\bar{Z}_a = 0.40$ (ρ_b = 70, 65, 60 mm), the samples standard deviation is $S = 5$ mm. Therefore, the type A uncertainty can be $u_A = \frac{5}{\sqrt{3}}$ mm. The combined uncertainty is $u_C = \sqrt{u_A^2 + u_B^2} = 6.42$ mm. Meanwhile, we calculated the λ_{I1} (maximum stretch of

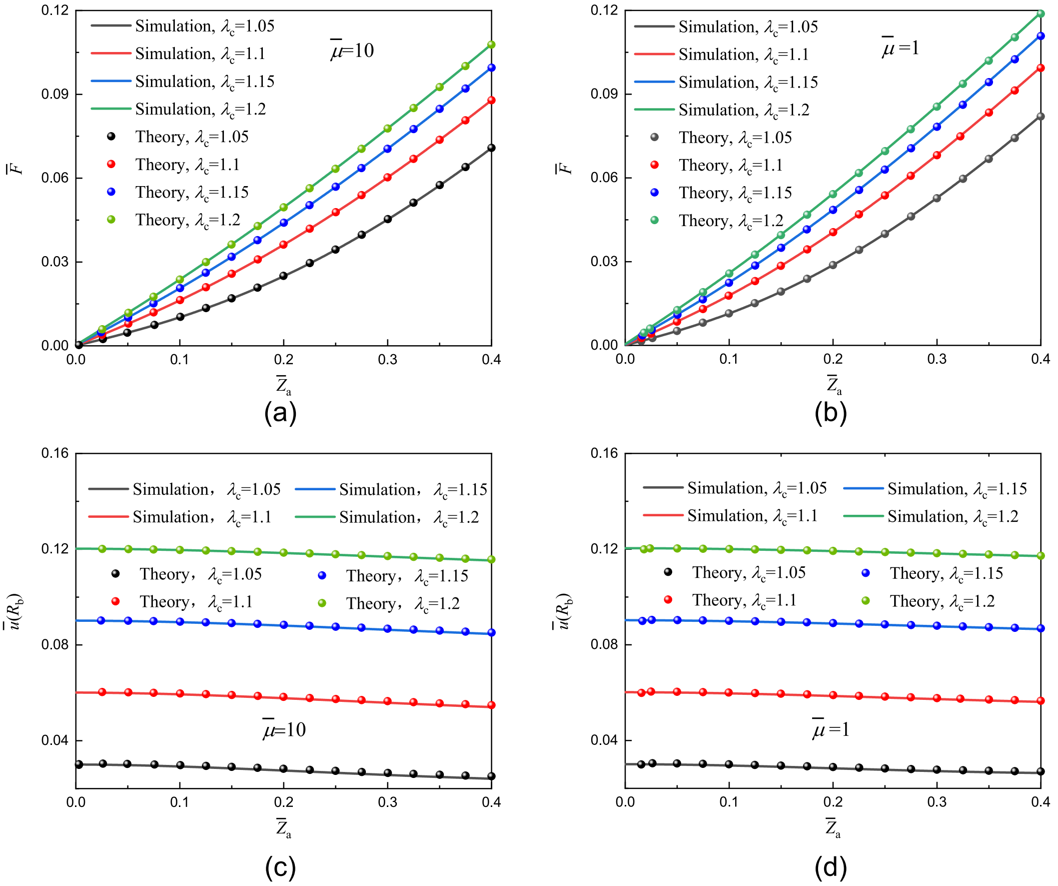

(a) (b)

(c) (d)

Fig. 4. Deformation of pre-stretched bilayer films: (a) and (b) are the force–displacement curves, representing $\bar{\mu} = 10$ and $\bar{\mu} = 1$. (c) and (d) are the displacement of point b, representing $\bar{\mu} = 10$ and $\bar{\mu} = 1$ respectively.

the film) at point a for $\bar{Z}_a = 0.30$, 0.35, 0.40, and 0.45, which are 1.29, 1.40, 1.52, and 1.69, respectively. This indicates that the films are subject to small and moderate deformations during the experiment. Since the theoretical framework and numerical simulations are established based on the neo-Hookean material model, the experimental results are agreement with theory and simulation. However, it should be noted that if the film undergoes larger deformation, our theoretical predictions may deviate.

5. Conclusions

This study investigates the blister deformation and subsequent delamination of a bilayer film subjected to shaft loading. We derive the axisymmetric equilibrium equations and boundary conditions governing deformation and solve the resulting differential equations to obtain deformation profiles. Theoretical predictions are validated by comparison with numerical simulations. The effects of varying layer modulus ratios and pre-stretched on deformation are examined, finding that bilayer films with SU-HL structure tend to compress or bend in the lower layer. Griffith's energy release rate is then employed to quantify the release rate and predict delamination, which are compared with simulation results. Regarding the influence of modulus ratio on delamination, HU-SL is more favorable at small $\bar{Z}_a$, whereas SU-HL is more suitable at larger $\bar{Z}_a$. Finally, delamination experiments are conducted to further validate the proposed framework. The theoretical framework and these findings provide guidance for the design of bilayer film structures.

CRediT authorship contribution statement

Ce Sun: Writing – original draft, Validation, Software, Methodology, Investigation, Formal analysis, Data curation, Conceptualization. **Jian Sun:** Writing – original draft, Methodology, Conceptualization. **Jinsong Leng:** Writing – original draft, Supervision, Conceptualization.

Declaration of competing interest

The authors declare that they have no known competing financial interests or personal relationships that could have appeared to influence the work reported in this paper.

Appendix A. Using of nonlinear elastic membranes theory

The theoretical framework of this study is based on membrane theory. Membrane theory typically assumes that the thickness of the membrane with respect to the radius $\frac{h}{R_c}$ is small and large tensile forces occur in the membrane during deformation, so we can neglect the bending stiffness and bending stresses and use the theory of non-linear elastic membranes [34,35]. Our study is similar to the indentation of suspended membranes. Prior studies on the indentation of suspended membranes have shown that if the suspended structure is a plate or a rigid membrane, bending and shear effects dominate only in the early stage of vertical displacement; as displacement increases, the response progressively transitions into a tensile-dominated regime [39]. For our manuscript, the membrane is considered extremely soft and very thin, making it easier to rapidly enter the tensile-dominated state. Thus,

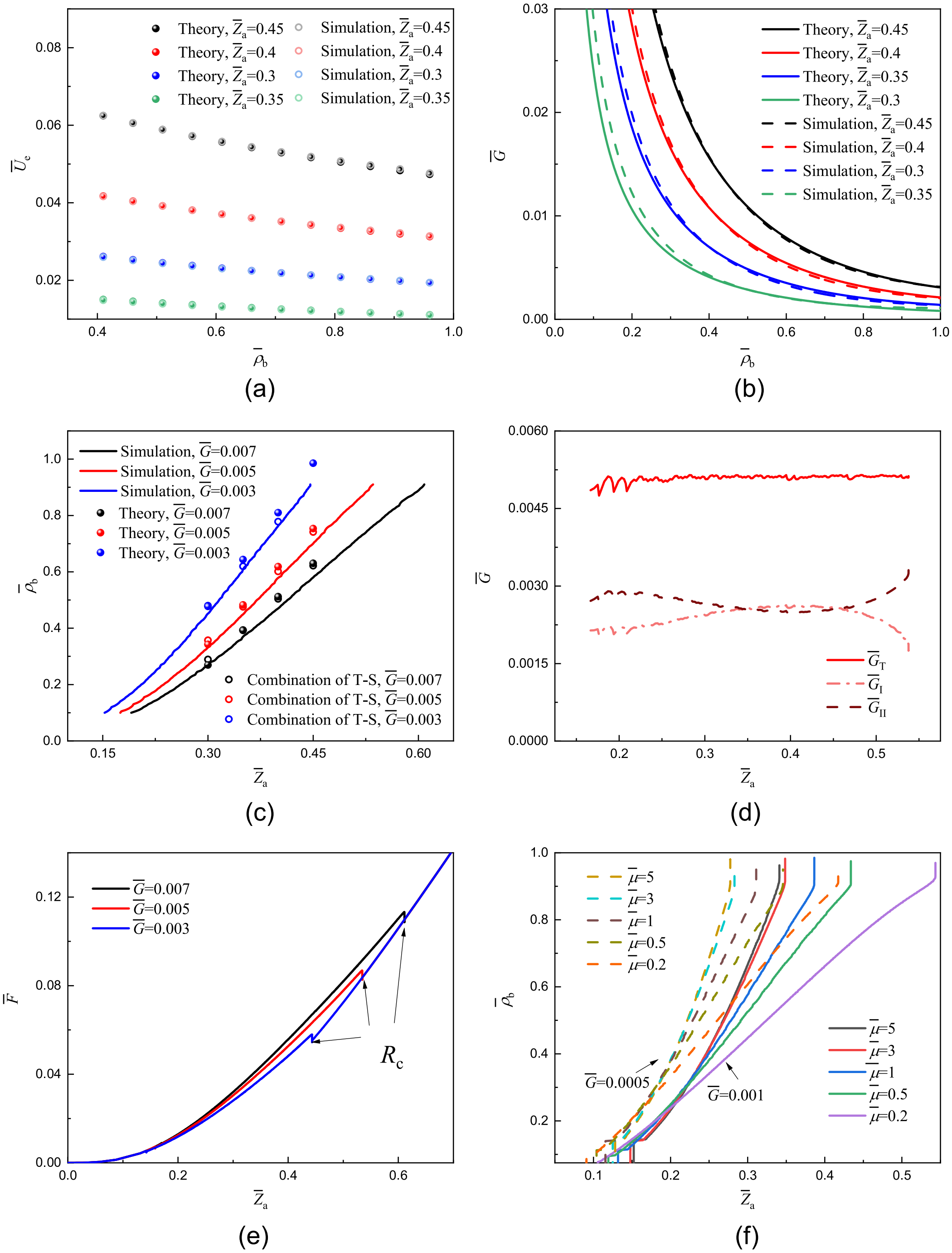

Fig. 5. (a) The relationship between $\bar{U}_e$ and $\bar{\rho}_b$ for $\bar{Z}_a$ = 0.3, 0.35, 0.4, and 0.45. (b) $\bar{G}$, derived from the derivative of $\bar{U}_e$ with respect to $\pi\bar{\rho}_b^2$. (c) Comparison of the predicted $\bar{\rho}_b$ from the theory and the T-S with the VCCT simulation. (d) The energy release rates of G_I, G_{II} and the total energy release rate $G_{equiv} = G_I + G_{II}$. (e) Force–displacement curves for different $\bar{G}$. (f) $\bar{\rho}_b$ for different $\bar{\mu}$, including HU-SL and SU-HL.

during most of the deformation process, large tensile forces prevail, and $\frac{h}{R_c}$ becomes a key parameter [35,40]. Therefore, we conducted numerical simulations on films with different thickness ratios ($\frac{h}{R_c}$ = 0.005, 0.01, 0.02, 0.05, 0.1) and extracted the corresponding force–displacement curves (see Fig. A.1). The results indicate that when $\frac{h}{R_c}$ ≤ 0.02, the impact of bending on overall deformation is minimal, and when $\frac{h}{R_c}$ approaches 0.01, there is almost no effect. Therefore, we believe that it is reasonable to consider the structure as a film within the range of $\frac{h}{R_c}$ ≤ 0.02. We have added these clarifications to the main text and appendix, explicitly noting that the governing equations neglect bending terms and are thus applicable to smaller $\frac{h}{R_c}$ and tensile-dominated membrane deformation. If bending effects are included, the governing equation for membrane deformation can be

$$(rT_1)' - r'T_2 + \kappa_1 rQ\sqrt{r'^2 + z'^2} = 0, \tag{A.1}$$

$$\kappa_1 T_1 + \kappa_2 T_2 - \frac{1}{r\sqrt{r'^2 + z'^2}}(rQ)' = 0, \tag{A.2}$$

$$(rM_1)' - r'M_2 - rQ\sqrt{r'^2 + '^2} = 0 \tag{A.3}$$

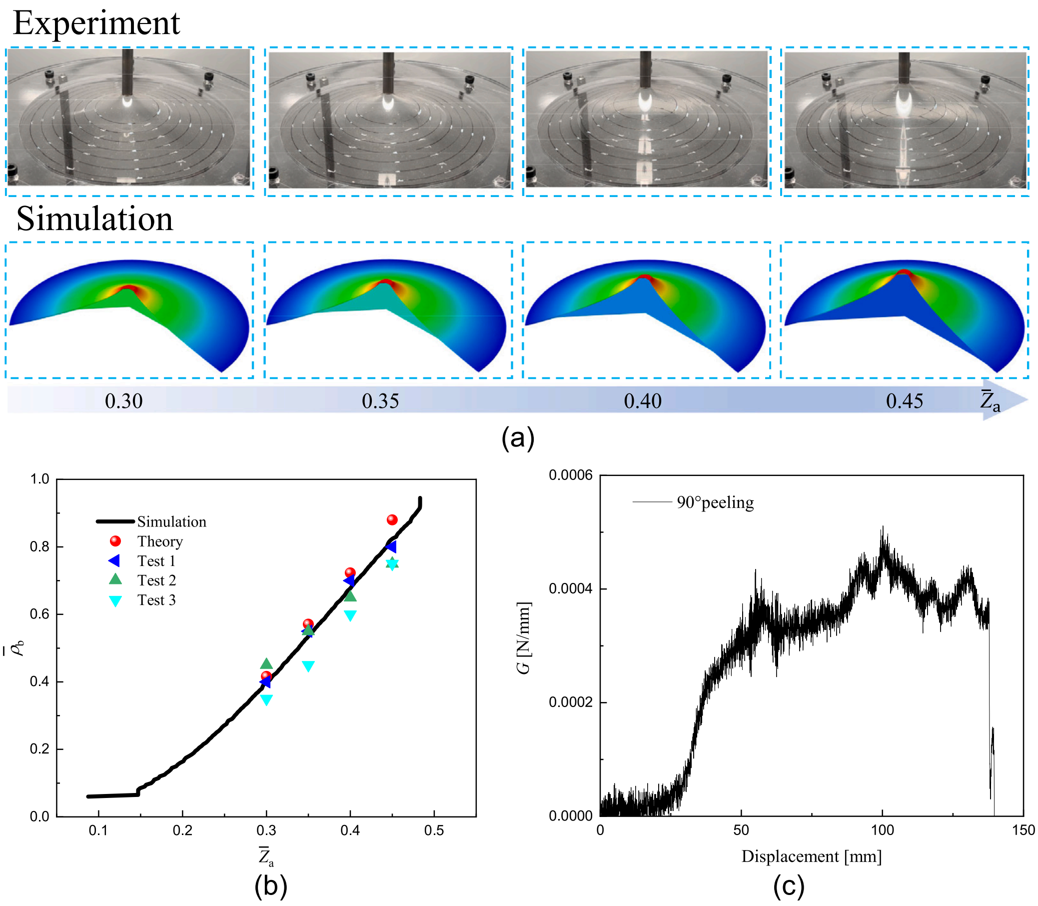

Fig. 6. Experimental results: (a) Delamination of the films for $\bar{Z}_a$ = 0.30, 0.35, 0.40, and 0.45. The top are the experimental results, and the bottom are the simulation results. (b) Delamination radius $\bar{\rho}_b$ from experiments, theory and simulation. (c) The critical energy release rate $\bar{G}_c$ obtained from 90° peeling test.

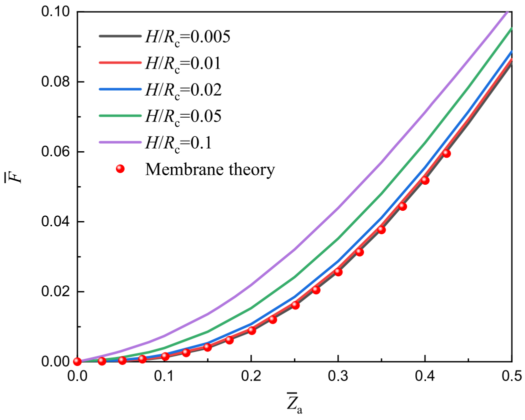

Fig. A.1. The force–displacement curves for $\frac{h}{R_c}$ = 0.005, 0.01, 0.02, 0.05, 0.1.

where M_1, M_2 are the bending moments in the corresponding directions and Q is the transverse stress resultant (shear stress). The first two equations are the force balances in the tangential and normal directions, with the third equation being the balance of bending forces. This case requires solving the fourth-order differential equation, which is more complex than the second-order differential equation that does not take bending into account. For a more detailed discussion, please refer to [41].

Appendix B. Boundary conditions

B.1. Segment ab

The boundary conditions at point a are defined as

$$r_{\rm I}(\rho_{\rm Ia}) = R_{\rm a}, \tag{B.1}$$

$$z_{\rm I}(\rho_{\rm Ia}) = Z_{\rm a}, \tag{B.2}$$

$$r'_{\rm I}(\rho_{\rm Ia}) = \lambda_{\rm I1}(\rho_{\rm Ia}) \cos \alpha_{\rm Ia}, \tag{B.3}$$

$$z'_{\rm I}(\rho_{\rm Ia}) = \lambda_{\rm I1}(\rho_{\rm Ia}) \sin \alpha_{\rm Ia}. \tag{B.4}$$

For computational convenience, the calculation can be started from the platen indenter by imposing $z_{\rm I}(\rho_{\rm Ia}) = 0$. In this case, $Z_{\rm a} = 0$ corresponds to the displacement at point a. The value $\lambda_{\rm I1}(\rho_{\rm Ia})$ is assigned as an initial value. By specifying $\lambda_{\rm I1}(\rho_{\rm Ia})$, one can search for an appropriate $\alpha_{\rm Ia}$ such that the boundary conditions for segment bc are satisfied. In fact, for any given pair of $\lambda_{\rm I1}(\rho_{\rm Ia})$ and $\alpha_{\rm Ia}$, the deformation of the membrane in segment ab can be determined.

B.2. Segment bc

Based on the solution for segment bc, the variables at point b are obtained as

$$r_{\rm I}(\rho_{\rm Ib}) = r_{\rm II}(\rho_{\rm IIb}) = r(\rho_{\rm b}), \tag{B.5}$$

$$z_{\rm I}(\rho_{\rm Ib}) = z_{\rm II}(\rho_{\rm IIb}) = z(\rho_{\rm b}), \tag{B.6}$$

$$r'_{\rm I}(\rho_{\rm Ib}) = \lambda_{\rm I1}(\rho_{\rm Ib}) \cos \alpha_{\rm Ib}, \tag{B.7}$$

$$z'_{\mathrm{I}}(\rho_{\mathrm{Ib}}) = \lambda_{\mathrm{I1}}(\rho_{\mathrm{Ib}})\sin\alpha_{\mathrm{Ib}}, \tag{B.8}$$

where subscript I refers to variables in segment ab, and II refers to those in segment bc.

The force equilibrium conditions at point b are expressed as

$$T_1(\rho_{\mathrm{IIb}}) + T_1(\rho_{\mathrm{Ib}})\cos\alpha_{\mathrm{Ib}} = T_1(\rho_{\mathrm{b}})\cos\alpha_{\mathrm{b}}, \tag{B.9}$$

$$T_1(\rho_{\mathrm{Ib}})\sin\alpha_{\mathrm{Ib}} = T_1(\rho_{\mathrm{b}})\sin\alpha_{\mathrm{b}}, \tag{B.10}$$

where ρ_{b} and α_{b} correspond to the information of the bilayer films at the right side of point b. Assuming continuity of the circumferential stretch at point b, therefore,

$$\lambda_2(\rho_{\mathrm{b}}) = \lambda_{\mathrm{I2}}(\rho_{\mathrm{Ib}}) = \lambda_{\mathrm{II2}}(\rho_{\mathrm{IIb}}). \tag{B.11}$$

At the left boundary of segment bc, we have

$$r'(\rho_{\mathrm{b}}) = \lambda_1(\rho_{\mathrm{b}})\cos\alpha_{\mathrm{b}}, \tag{B.12}$$

$$z'(\rho_{\mathrm{b}}) = \lambda_1(\rho_{\mathrm{b}})\sin\alpha_{\mathrm{b}}. \tag{B.13}$$

With Eqs. (B.5), (B.6), (B.12) and (B.13) as the boundary conditions, the governing equation can be solved again, which allows for the computation of $\lambda_2(\rho_{\mathrm{c}})$. The solution is considered complete when $\lambda_2(\rho_{\mathrm{c}})$ is sufficiently close to 1. Otherwise, the initial input α_{Ia} should be adjusted and the solution process repeated, until a suitable α_{Ia} is found such that $\lambda_2(\rho_{\mathrm{c}})$ is sufficiently close to 1. Notably, the key premise of this solution procedure is that the lower film segment bd remains in tension.

Appendix C. Simulation setting

The numerical simulation in this article was conducted using Abaqus 2024. It mainly focuses on two cases: (i) $\bar{\rho}_{\mathrm{b}}$ is a constant that does not vary with $\bar{Z}_{\mathrm{a}}$, and the delamination boundary no longer expands further. (ii) $\bar{\rho}_b$ is a variable that changes continuously with $\bar{Z}_{\mathrm{a}}$, and the delamination boundary continues to expand. Both cases were modeled using an axisymmetric model, with the upper and lower films set to a thickness of 0.5 and a radius of 100, using a neo-Hookean hyperelastic constitutive model and quasi-static simulation. Fixed constraints were applied at the circumference of the films, and a vertical displacement loading zone with a radius of 5 was set in the center region of the upper film. Five elements were set in the vertical direction of the films.

For case (i), 220 elements were set in the horizontal direction of the upper film, including 20 refined elements at the loading boundary and $\bar{\rho}_{\mathrm{b}}$, while 210 elements were set in the horizontal direction of the lower film, including 10 refined elements at $\bar{\rho}_{\mathrm{b}}$.

For case (ii), 210 elements were set in the horizontal direction of the upper film, including 10 refined elements at the loading boundary of the upper film, and 200 elements were set in the horizontal direction of the lower film. The 8-node biquadratic axisymmetric quadrilateral element was used and mixed simplified integral was adopted. We used virtual crack closure technology (VCCT) for numerical simulation, setting microcracks between the two layers of the film and defining the crack propagation path. We employed the BK criterion for the fracture criterion, which is [42]

$$G_{\mathrm{equivC}} = G_{\mathrm{Ic}} + (G_{\mathrm{IIc}} - G_{\mathrm{Ic}})\left(\frac{G_{\mathrm{II}}}{G_{\mathrm{I}} + G_{\mathrm{II}}}\right)^{\eta}. \tag{C.1}$$

Among them, G_{equivC} is the mixed critical energy release rate, G_{Ic} is the critical energy release rate for mode I fracture, G_{IIc} is the critical energy release rate for mode II fracture, and G_{I} and G_{II} are the energy release rates for mode I and mode II, respectively. G_{I} and G_{II} are calculated based on the displacements of the crack tip nodes and the nodal forces. η is a material parameter. The mixed energy release rate $G_{\mathrm{equiv}} = G_{\mathrm{I}} + G_{\mathrm{II}}$, and fracture occurrence is judged by $1 < G_{\mathrm{equiv}}/G_{\mathrm{equivC}} < 1 + f_{\mathrm{tol}}$, where f_{tol} is referred to as the tolerance parameter to ensure that the model can converge. It is usually set to 0.2, but in order to improve computational accuracy, we uniformly set this value to 0.03 while ensuring convergence. In simulations, G_{equivC} is equal to the parameter G_{c} used in theory. In theory, we calculated the total energy release rate using Eq. (9), and determined whether delamination occurs by checking if G is greater than or equal to G_{c}. In simulations, delamination is determined by whether G_{equiv} is greater than or equal to G_{equivC}. In the numerical simulations, we set $G_{\mathrm{Ic}} = G_{\mathrm{IIc}}$ consistent with [43,44]. Therefore, $G_{\mathrm{equivC}} = G_{\mathrm{Ic}}$, so G_{equivC} is equal to G_{c} used in the theory.

In Fig. 5(d), the solid curve represents the total energy release rate $\bar{G}_{\mathrm{equiv}}$, while the dashed curve and dotted curve correspond to mode I (open) and mode II (shear) components, $\bar{G}_{\mathrm{I}}$ and $\bar{G}_{\mathrm{II}}$, respectively. Although $\bar{G}_{\mathrm{equiv}}$ is nearly constant, the relative contributions of $\bar{G}_{\mathrm{I}}$ and $\bar{G}_{\mathrm{II}}$ evolve with increasing $\bar{Z}_{\mathrm{a}}$, indicating a transition in the dominant fracture mode. At the onset of delamination, $\bar{G}_{\mathrm{II}}$ exceeds $\bar{G}_{\mathrm{I}}$, reflecting shear-dominated behavior due to an initially small peeling angle. As $\bar{Z}_{\mathrm{a}}$ and $\bar{\rho}_{\mathrm{b}}$ increase, the peeling angle increases, and the fracture mode gradually shifts toward opening, with $\bar{G}_{\mathrm{I}}$ eventually exceeding $\bar{G}_{\mathrm{II}}$. Near the boundary, another transition occurs due to radial-displacement constraints at the edge. Fig. 5(d) shows that $\bar{G}_{\mathrm{equiv}}$ remains essentially constant, supporting the assumption $\bar{G} = \bar{G}_{\mathrm{c}}$ for quasi-static case. A more comprehensive investigation of fracture mode effects will be pursued in future work.

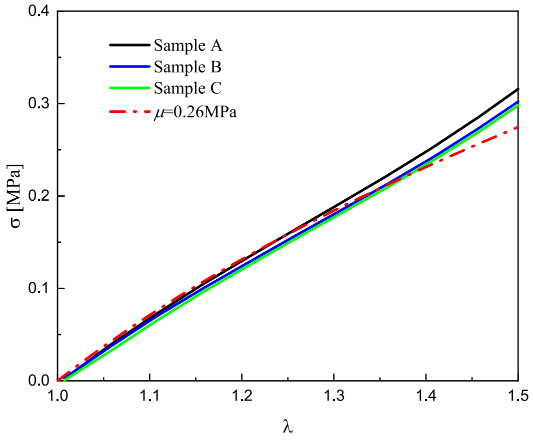

Fig. D.1. The force–displacement curves of tape film tensile.

Appendix D. Experiment of film tensile and 90° peeling

The tensile testing machine Shimadzu AGS-X series (100 N range) was used in films tensile test. The PDMS films were prepared as 130 mm × 20 mm tapes. The stretching curves of the films are shown by the solid curves in Fig. D.1 and the dotted curve represents $\mu = 0.26$ MPa.

For 90° peeling, the bilayer films were prepared as 110 mm × 20 mm tapes. In this test, the lower film was attached to a rigid substrate, while the upper film is affixed with a non-stretchable and flexible backing, one end of which is connected to a 1000 mm long, inextensible thin string, serving as the peeling arm for the 90° peel test. This method was proposed by Li et al. [45]. The peeling force–displacement curve is shown in Fig. D.2. G_{c} can be calculated by dividing the peeling force by the width of the film (20 mm). The result of 90° peeling tests on the bilayer films, which range from 0.00026 to 0.0005 N/mm, is shown as Fig. 6(c).

Appendix E. Supplementary data

Supplementary material related to this article can be found online at https://doi.org/10.1016/j.eml.2026.102458.

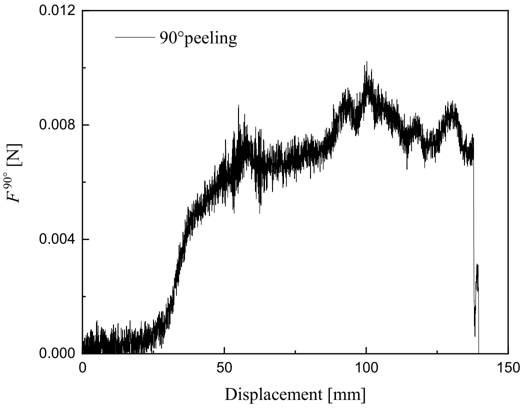

Fig. D.2. The force–displacement curve of 90° peeling.

Data availability

Data will be made available on request.

References

[1] R. Yan, Z. Xu, H. Yi, C. Xu, H. Xu, X. Qi, X. Dong, C. Hu, Z. Li, X. Jiang, Bioinspired Janus universal adhesive patch: Bridging the contrasting interface of soft tissues and medical devices, Adv. Funct. Mater. (2025) 2422130.

[2] M. Wilkins, A. Blaurock, D. Engelman, Bilayer structure in membranes, Nat. New Biol. 230 (11) (1971) 72–76.

[3] E. Song, Y.K. Lee, R. Li, J. Li, X. Jin, K.J. Yu, Z. Xie, H. Fang, Y. Zhong, H. Du, et al., Transferred, ultrathin oxide bilayers as biofluid barriers for flexible electronic implants, Adv. Funct. Mater. 28 (12) (2018) 1702284.

[4] E. Song, H. Fang, X. Jin, J. Zhao, C. Jiang, K.J. Yu, Y. Zhong, D. Xu, J. Li, G. Fang, et al., Thin, transferred layers of silicon dioxide and silicon nitride as water and ion barriers for implantable flexible electronic systems, Adv. Electron. Mater. 3 (8) (2017) 1700077.

[5] T. Li, J. Sun, J. Leng, Y. Liu, An electrical heating shape memory polymer composite incorporated with conductive elastic fabric, J. Compos. Mater. 56 (11) (2022) 1725–1736.

[6] L. Xu, J. Zhang, J. Luo, Y. Cui, J. Chen, B. Zeng, Z. Deng, L. Shao, "Double-sided protector" Janus hydrogels for skin and mucosal wound repair: applications, mechanisms, and prospects, J. Nanobiotechnology 23 (1) (2025) 1–40.

[7] F. Wang, W. He, B. Dai, X. Zhang, Y. Wen, Recent advances in asymmetric wettability dressings for wound exudate management, Research 8 (2025) 0591.

[8] Z. Zhu, Z. Yang, Y. Xia, H. Jiang, A review of debonding behavior of soft material adhesive systems, Mech. Soft Mater. 4 (1) (2022) 7.

[9] K. Kendall, Thin-film peeling-the elastic term, J. Phys. D: Appl. Phys. 8 (13) (1975) 1449.

[10] V.A. Eremeyev, K. Naumenko, A relationship between effective work of adhesion and peel force for thin hyperelastic films undergoing large deformation, Mech. Res. Commun. 69 (2015) 24–26.

[11] L. He, J. Lou, S. Kitipornchai, J. Yang, J. Du, Peeling mechanics of hyperelastic beams: Bending effect, Int. J. Solids Struct. 167 (2019) 184–191.

[12] M. Ceglie, N. Menga, G. Carbone, Modelling the non-steady peeling of viscoelastic tapes, Int. J. Mech. Sci. 267 (2024) 108982.

[13] Z. Zhu, Y. Xia, C. Jiang, Z. Yang, H. Jiang, Investigation of zero-degree peeling behavior of visco-hyperelastic highly stretchable adhesive tape on rigid substrate, Eng. Fract. Mech. 241 (2021) 107368.

[14] Y. Wei, H. Zhao, Peeling experiments of ductile thin films along ceramic substrates–Critical assessment of analytical models, Int. J. Solids Struct. 45 (13) (2008) 3779–3792.

[15] Y. Wei, J.W. Hutchinson, Interface Strength, Work of Adhesion and Plasticity in the Peel Test, Springer, 1998.

[16] Q. Yang, M. Thouless, S. Ward, Numerical simulations of adhesively-bonded beams failing with extensive plastic deformation, J. Mech. Phys. Solids 47 (6) (1999) 1337–1353.

[17] F. Zhang, D. Li, C. Wang, Z. Liu, M. Yang, Z. Cui, J. Yi, M. Wang, Y. Jiang, Z. Lv, et al., Shape morphing of plastic films, Nat. Commun. 13 (1) (2022) 7294.

[18] J. Chen, H. Ruan, X. Ju, Y. Xu, X. Chen, C. Pan, L. Liang, A pre-tension based adhesion-tuning approach: Bridging the gap in peeling test research and application, Eng. Fract. Mech. 319 (2025) 110980.

[19] M.R. Begley, R.R. Collino, J.N. Israelachvili, R.M. McMeeking, Peeling of a tape with large deformations and frictional sliding, J. Mech. Phys. Solids 61 (5) (2013) 1265–1279.

[20] G. Yang, K. Zhu, W. Guo, D. Wu, X. Quan, X. Huang, S. Liu, Y. Li, H. Fang, Y. Qiu, et al., Adhesive and hydrophobic bilayer hydrogel enabled on-skin biosensors for high-fidelity classification of human emotion, Adv. Funct. Mater. 32 (29) (2022) 2200457.

[21] J. Deng, M. Hu, Z. Cai, W. Yu, L. Zhan, X. Zhu, Q. Ke, R. Gao, X. Zhou, H. Liu, et al., A highly stable, multifunctional Janus dressing for treating infected wounds, Adv. Healthc. Mater. 13 (27) (2024) 2401345.

[22] H. Yin, Z. Wang, Y. Jiao, Y. Zhang, Y. Ma, X. Feng, Interfacial competing fracture in peeling of bi-interface film-substrate system, J. Mech. Phys. Solids (2025) 106216.

[23] W. Jian, H. Yin, Y. Chen, X. Feng, Competing behavior of interface delamination and wafer cracking during peeling film from ultra-thin wafer, Int. J. Solids Struct. 305 (2024) 113058.

[24] S. Jain, T. Yang, M. Negley, S.R. Na, K.M. Liechti, R.T. Bonnecaze, A parametric cohesive zone beam theory analysis of mixed-mode graphene transfer, Int. J. Adhes. Adhes. 89 (2019) 129–138.

[25] H. Yin, Y. Yao, Y. Yang, Z. Peng, S. Chen, Interfacial competitive debonding of a bilayer elastic film on a rigid substrate, J. Appl. Mech. 89 (1) (2022) 011003.

[26] S. Heide-Jørgensen, M.K. Budzik, Effects of bondline discontinuity during growth of interface cracks including stability and kinetic considerations, J. Mech. Phys. Solids 117 (2018) 1–21.

[27] C.-S. Shen, H.-F. Wang, C.-L. Du, Peeling of a film from a flexible cantilever substrate, Mech. Res. Commun. 119 (2022) 103833.

[28] C.-S. Shen, F. Yao, B. Zhou, B. Li, H.-F. Wang, Multi-peeling states of elastic film from flexible substrate, Int. J. Solids Struct. 256 (2022) 111949.

[29] Z. Dai, D.A. Sanchez, C.J. Brennan, N. Lu, Radial buckle delamination around 2D material tents, J. Mech. Phys. Solids 137 (2020) 103843.

[30] Z. Dai, N. Lu, Poking and bulging of suspended thin sheets: Slippage, instabilities, and metrology, J. Mech. Phys. Solids 149 (2021) 104320.

[31] X. Yang, L. Yu, R. Long, Contact mechanics of inflated circular membrane under large deformation: Analytical solutions, Int. J. Solids Struct. 233 (2021) 111222.

[32] R. Long, C.-Y. Hui, Axisymmetric membrane in adhesive contact with rigid substrates: Analytical solutions under large deformation, Int. J. Solids Struct. 49 (3–4) (2012) 672–683.

[33] G.A. Holzapfel, Nonlinear solid mechanics: a continuum approach for engineering science, 2002.

[34] A.M. Kolesnikov, Ball indentation of perforated circular hyperelastic membranes, in: Sixty Shades of Generalized Continua: Dedicated to the 60th Birthday of Prof. Victor A. Eremeyev, Springer, Switzerland, 2023, pp. 389–400.

[35] A. Libai, J. Simmonds, The Nonlinear Theory of Elastic Shells, second ed., Cambridge University Press, UK, 1998.

[36] S.P. Pearce, J.R. King, M.J. Holdsworth, Axisymmetric indentation of curved elastic membranes by a convex rigid indenter, Int. J. Non-Linear Mech. 46 (9) (2011) 1128–1138.

[37] M.D. Bartlett, S.W. Case, A.J. Kinloch, D.A. Dillard, Peel tests for quantifying adhesion and toughness: A review, Prog. Mater. Sci. 137 (2023) 101086.

[38] Z. Shi, P. Chen, Z. Wu, Y. Wang, Z. Li, Evaluation on VCCT-like methods in hyperelastic materials.

[39] K.-T. Wan, Fracture mechanics of a shaft-loaded blister test–transition from a bending plate to a stretching membrane, J. Adhes. 70 (3–4) (1999) 209–219.

[40] O. Scott, M. Begley, U. Komaragiri, T. Mackin, Indentation of freestanding circular elastomer films using spherical indenters, Acta Mater. 52 (16) (2004) 4877–4885.

[41] S.P. Pearce, J.R. King, T. Steinbrecher, G. Leubner-Metzger, N.M. Everitt, M.J. Holdsworth, Finite indentation of highly curved elastic shells, Proc. R. Soc. A: Math. Phys. Eng. Sci. 474 (2209) (2018) 20170482.

[42] X. Li, P. Qu, H. Kong, Y. Zhu, C. Hua, A. Guo, S. Wang, Multi-scale numerical analysis of damage modes in 3D stitched composites, Int. J. Mech. Sci. 266 (2024) 108983.

[43] Y. Hu, J. Leng, F. Jia, Y. Liu, Peeling behavior of a film on inner surface of a tube, Extrem. Mech. Lett. 58 (2023) 101930.

[44] Z. Zhu, Z. Yang, F. Yang, C. Yao, H. Jiang, Enhancing interfacial shear debonding resistance by mechanical mismatch, Int. J. Mech. Sci. 260 (2023) 108656.

[45] Q. Li, W. Liu, C. Yang, P. Rao, P. Lv, H. Duan, W. Hong, Kirigami-inspired adhesion with high directional asymmetry, J. Mech. Phys. Solids 169 (2022) 105053.